Shen Y, Li J, Freddi F, Igarashi A, Zhou J.(2022). Numerical investigation of transverse steel damper (TSD) seismic system for suspension bridges considering pounding between girder and towers. Soil Dynamic and Earthquake Engineering, 155: 107203. https://doi.org/10.1016/j.soildyn.2022.107203.

Numerical investigation of transverse steel damper (TSD) seismic system for suspension bridges considering pounding between girder and towers

Yu Shen[a], Jianzhong Li[a], Fabio Freddi[b], Akira Igarashi[c], and Jian Zhou[c]

[a]*State Key Laboratory of Disaster Reduction in Civil Engineering, Tongji University, Shanghai 200092, China*
[b]*Dept. of Civil, Environmental and Geomatic Engineering, University College London, London WC1E 6BT, UK*
[c]*Disaster Prevention Research Institute, Kyoto University, Gokasho, Uji-shi, Kyoto 611-0011 Japan.*

ABSTRACT

Transverse steel damper (TSD) is a promising passive control device used for seismic isolation and has been validated to feasibly balance the girder transverse seismic displacement and inertial force in cable-stayed bridges. However, for the TSD system, transverse pounding could occur at the locations of girder and tower legs when the gap size is insufficient to accommodate the girder-support transverse relative displacement under major earthquakes. Transverse pounding can significantly affect the dynamic responses of bridge structures, hence, the present paper investigates the effectiveness of TSD as a control strategy for transverse seismic responses in long-span bridge structures (*i.e.*, suspension bridges), accounting also for the influence of the pounding effect in the dynamic response analysis. A typical suspension bridge is considered for case study purposes, and four transverse girder-support connection systems are investigated, including the conventional fixed and sliding-free connections and the TSD connections with and without pounding effect. A comprehensive comparison of the seismic performance among these transverse restraining systems is conducted through Incremental Dynamic Analysis and fragility analysis. Additionally, the effect of seismic-induced pounding in the TSD system is assessed from an energetic point of view. The results show that, for the suspension bridge with TSDs as the transverse control strategy, a satisfactory balance between force and displacement demands can be obtained in small- to medium-intensity earthquakes. However, the pounding between the girder and tower legs during large-intensity earthquakes can substantially increase the seismic demands in the tower legs.

Keywords: Suspension bridges; Transverse steel damper system; Pounding response; Incremental dynamic analysis; Fragility curves; Seismic assessment

1. Introduction

Sliding-free or fixed girder-support connection systems are widely adopted in the transverse direction for long-span suspension or cable-stayed bridges to withstand the transverse seismic excitations [1,2]. For bridges located in low seismicity regions, the Transverse Sliding-Free (TSF) system is an advisable option since the seismic induced girder-support relative displacements are usually moderate. Conversely, in areas characterized by moderate to high seismic intensities, the displacements between girders and supports may exceed the displacement capacity of the bearings with consequent unseating [3]. In such situations, the Transverse Fixed (TF) system is usually adopted. Although the TF system allows limiting the girder-support relative displacements, several aspects require particular attention: *1)* piers and their footings must be designed to resist large transverse seismic force, which is not cost-effective; *2)* bearings, piers, and foundations may suffer damage when the seismic excitations exceed the design level [4,5].

Neither TSF nor TF can well balance the girder-support relative displacement and the internal seismic force at the same time. There is a trade-off between the internal forces of bridge tower and girder-support relative displacement for long-span bridges under moderate to high transverse earthquakes. To this end, different kinds of passive seismic control devices have been proposed, such as Frictional Pendulum Bearing [6,7], Viscous Fluid Damper (VFD) [8,9], and Yielding Metallic Damper [10,11]. Extensive numerical and experimental work has been carried out to validate the effectiveness of these devices [12,13]. However, most of these girder-support connection devices are merely implemented in the longitudinal direction of bridges, and only a few studies focused on the development of transverse isolation strategies for long-span bridges. Yan *et al.* [9] investigated the use of VFD as energy-dissipation devices installed at girder-support locations to help mitigate the transverse seismic force of cable-stayed bridges. Results showed that, under service loads, VFD could not accommodate the longitudinal movement of the girder unless ‘special’ and complex details are employed. The early development of Triangular Metallic Dampers (TADAS) mostly focused on their use in building structures [14,15] while their use in the transverse connection of bridges was only investigated in the last decade [16,17]. Camara [16] proposed the use of the TADAS as the deck-tower connection for controlling the transverse seismic motion of long-span cable-stayed bridges and prevent damage to tower legs [17]; however, how to reduce the interplay between longitudinal and transverse motions in this system was not mentioned. Actually, decoupling the transverse motion from the longitudinal displacement of bridges is a key issue for the employment of various seismic control devices. A few applications exist in practice, such as the Rion-Antirion cable-stayed bridge, where VFDs have been successfully used for the transverse isolation; however, their use required a complex and costly structural configuration [8,18,19]. To deal with these shortcomings, Shen *et al.* [3,20] concentrated in detailing the top connection of the vertical steel plates and the girder, and developed the Transverse Steel Damper (TSD) girder-support connection system for long-span cable-stayed bridges. This TSD can accommodate the longitudinal movement of the girder without deterioration of energy dissipation capacity in the transverse direction. Subsequently, its efficiency and reliability were validated by a series of shake table tests on a reduced scaled model bridge under near- and far-fault transverse ground motions [21,22]. Nevertheless, the use of TSD for seismic isolation in suspension bridges has not been extensively investigated.

The use of passive seismic control devices increases the girder-support relative displacement compared with TF system [23], leading to a higher risk of pounding between adjacent structure segments. Post-earthquake field investigations highlighted that pounding might cause considerable damage or even the collapse of colliding structures [24-26], and several studies focused on this research area. Nevertheless, to the authors' best knowledge, most of them focused on the pounding phenomenon of simply supported or continuous beam bridges [27,28]. It has seldom been seen in the literature that the pounding effects are included in the seismic analysis of long-span bridges. Shen *et al.* [29] investigated the effect of pounding on the longitudinal seismic demand of a cable-stayed bridge and its approach spans. It was found that the contact between these two structural systems has a relatively long duration, which caused a substantial increase in displacement demands of the approach spans. A similar phenomenon was observed by Deng *et al.* [30] while investigating long-span suspension bridge systems. Apart from the pounding between the main girder and adjacent approach spans along the longitudinal direction of bridges, the tower-girder pounding could also occur when the ground motions act in the transverse direction. As indicated by Camara [16], the definition of the contact between the girder and the towers is essential to simulating the realistic transverse connection for cable-stayed bridges. Tower-girder transverse pounding has been observed on the Yokohama Bay Bridge wind tongue during the 2011 Great East Japan Earthquake. Tomoaki *et al.* [31] numerically reproduced this pounding phenomenon and confirmed that pounding force might have caused severe damage to the wind tongue, thus highlighting the potential impact of transverse pounding between girder and towers during severe earthquakes, especially for near-field cases.

The present paper investigates the transverse seismic response of suspension bridges with the TSD girder-support connection system under near-fault earthquakes taking into account the pounding phenomenon between girder and tower columns. The motivations of this study are: *1)* not limited to evaluating the effect of pounding occurring between the deck and the towers but on the assessment of the transverse seismic performance of suspension bridges equipped with TSD devices; *2)* validating the effectiveness of TSD systems to collaborate strength, stiffness, and ductility of suspension bridges; and *3)* highlighting that the use of TSD devices is beneficial to retrofitting existing suspension bridges that are designed with considering transverse free connection and only leaving a limited girder-tower separation distance.

To this end, a simple numerical procedure for the definition of the key parameters controlling TSD hysteretic behavior is first introduced and validated. Then, a typical suspension bridge is considered for case study purposes, and four transverse girder-support connection systems are investigated, including the conventional TSF and TF systems and the TSD connections with and without pounding effect. Detailed finite element models have been developed for the bridge, including detailed modeling of the TSD and nonlinear contact element. The effectiveness of TSD in controlling the transverse seismic response of suspension bridges and the effect of pounding between the girder and towers on the performance of the TSD system are investigated by Incremental Dynamic Analyses (IDA), accounting for the influence of the uncertainty related to the earthquake input, *i.e.*, the record-to-record variability. Fragility curves are successively derived for several damage states providing valuable insights on the influence of the TSD system on the seismic response. Peak Ground Acceleration (PGA) is used as Intensity Measure (IM) in the analyses while considering both the selected ground motions' horizontal and vertical accelerations components. Both global and local level Engineering Demand Parameters (EDPs) [32,33], including displacements, relative displacements, curvature ductility demands, and shear forces at section level, are used in the analysis. Finally, energy analysis is performed on the TSD system to shed light on the mechanism of transverse pounding effects.

2. Transverse Steel Damper (TSD) system

Fig. 1 shows a girder-support connection system in which the TSD system controls the transverse horizontal behavior while the sliding bearings support the vertical loads of the suspended superstructure. The developments of TSD in bridges were pursued to a simple and reliable transverse seismic-control system that exhibits superior seismic behavior comparable to mature damper systems employed in buildings [34-36]. The detailed configuration of the TSD is illustrated in Fig. 2. It comprises triangular steel plates, steel hemispheres, an upper plate with grooves, and a lower plate. Polytetrafluoroethylene (PTFE) slides are attached to the groove surfaces to ensure that hemispheres can slide freely in the longitudinal direction, thus decoupling the transverse and the longitudinal degree of freedom of the TSD. The upper plate and hemispheres are designed to be sufficiently stiff to provide the transverse load path for the inertial force of the main girder, which is transferred through triangular plates to the lower strut under transverse seismic actions. Eventually, this internal force is transferred to the tower columns.

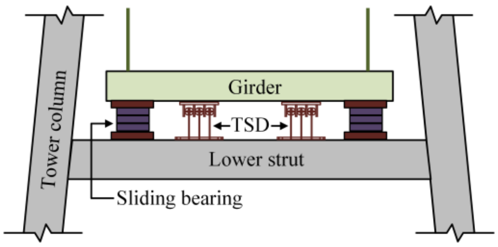

Fig. 1. Schematic of the transverse TSD girder-support connection system.

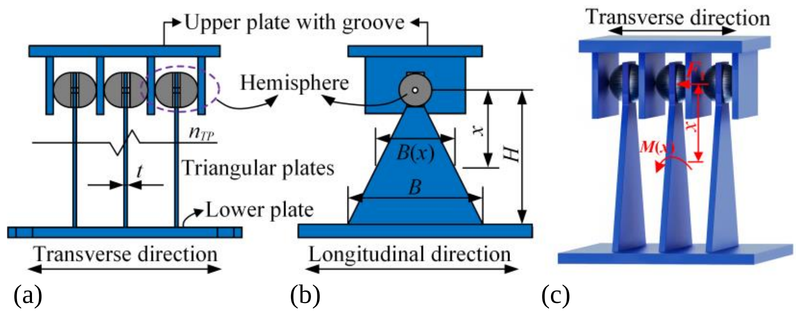

Fig. 2. Configurations and details of the Transverse Steel Damper (TSD): (a) front elevation; (b) side elevation; and (c) 3D graph.

The force-displacement relationship of TSD can be described by the Bouc-Wen hysteretic model [37], as shown in Fig. 3(a). In which, the model parameters of yielding force, F_y, and yielding displacement, D_y, are determined based on the material properties, triangular steel plate's dimensions, and number with Equations (1) and (2), respectively [3].

$$F_y = n_{TP} \frac{Bt^2 \sigma_y}{6H} \tag{1}$$

$$D_y = \frac{6F_y H^3}{n_{TP} EBt^3} \tag{2}$$

where t is the thickness of one triangular steel plate (see Fig. 2(a)); n_{TP} is the number of steel plates; B and H are respectively the bottom width and height of the triangular steel plates (see Fig. 2(b)); σ_y and E are respectively the yield stress and elastic modulus of steel.

Combining Equations (1) and (2) gives the initial stiffness of TSD, K_1:

$$K_1 = \frac{F_y}{D_y} = n_{TP} \frac{EBt^3}{6H^3} \tag{3}$$

The post-yielding stiffness K_2 can be described mathematically as:

$$K_2 = \frac{F_u - F_y}{D_u - D_y} \tag{4}$$

where D_u is the ultimate displacement of TSD, defined as the deflection of TSD when the hemispheres separate from the grooves during the transverse motion, and F_u is the force value corresponding to D_u. Based on the statistical analysis, the hardening ratio of the TSD (*i.e.*, K_2/K_1) can be approximately expressed as [38]:

$$K_2 / K_1 = 0.00433 \times \frac{BH - 0.357B + 0.1891}{t - 0.003} \tag{5}$$

The above-described numerical procedure for the definition of the force-displacement relationship of TSD has been validated against cyclic test results of full-scale TSDs performed by Shen *et al.* [3] As shown in Figs. 3(b) and (c), the monotonic and cyclic responses of the Bouc-Wen model with an exponent $\xi = 10$ (used to control the transition from elastic to plastic branches) provide a good match with the experimental results.

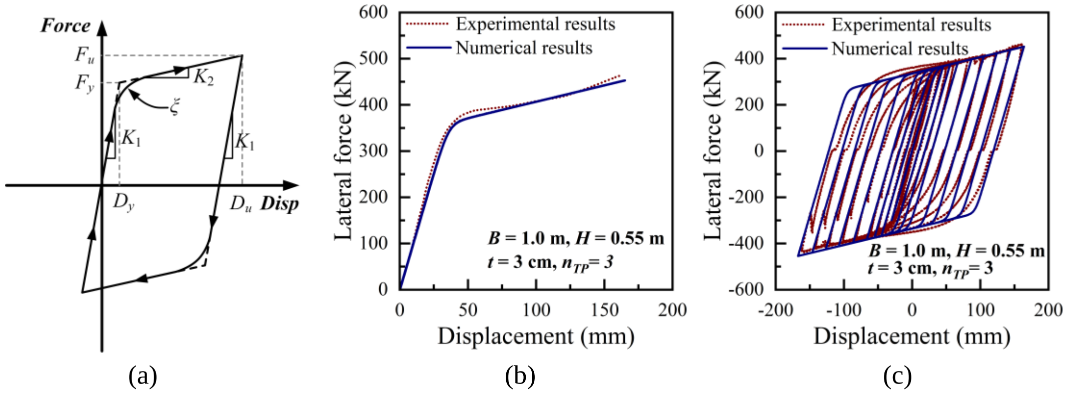

Fig. 3. Modelling and validation of the force-displacement behavior for Transverse Steel Damper (TSD): (a) the Bouc-Wen hysteretic model; (b) monotonic response curves; and (c) cyclic response curves.

3. Bridge prototype and ground motions set

3.1 Bridge prototype

The three-tower four-span suspension bridge shown in Fig. 4 is chosen for case study purposes. The bridge is symmetrically provided with two ends supporting two-column bents and has a total length of 620 m, with two main spans of 220 m and two back spans of 90 m. A steel-concrete composite girder (see Section A-A in Fig. 4), with a width and a depth of 34.5 and 3.5 m, respectively, is suspended by 132 steel hangers on each side at 8 m intervals. The two main suspension cables are parallel and continuous, supported by saddles at the towers, and have their ends fixed to either end of the stiffening girder. The maximum cable sag at the two main spans is 44 m, resulting in a rise-span ratio of 1/5. Three identical H-shaped reinforced concrete towers are employed to carry the vertical load transmitted by saddles, and each of the three towers has a height of 96 m, including a 15 m top decoration portion. Tower legs are vertical and connected by a lower strut, which has a section of 5.6 m × 3.0 m at the mid-strut in the transverse direction (see Section G-G in Fig. 4). Each tower leg can be subdivided into two segments: the upper (the leg above the lower strut - height of 58 m) and the lower segment (the leg below the lower strut - height of 23 m). An approximatively rectangular box shape is adopted for tower legs, and the sectional dimensions gradually reduce with the height, as shown by Sections B-B to F-F in Fig. 4. The girder is continuously supported at the lower struts, and a transverse gap of 0.5 m is provided between the edges of the girder and the tower legs for service conditions. In addition, all tower legs and bridge bents use pile foundations with a pile cap for a total of fifteen and six piles per tower leg and bent column, respectively.

This bridge is designed according to CJJ 166-2011 [39] and JTG/T B02-01-2008 [40] with the seismic design category A and a site class II. According to the design requirements, the bridge shall resist the seismic loading corresponding to a 2% probability of exceedance in 50 yrs (*i.e.*, maximum considered earthquakes, MCE) with only minor local damage. Detailed reinforcements are provided at the critical regions of some components that are expected to experience local damage (*i.e.*, plastic hinges) according to the capacity design philosophy [39,41,42]. C50 concrete (*i.e.*, compressive strength of 50 MPa) and Q400 steel rebars (*i.e.*, yield strength of 400 MPa) are used for the towers and supporting bents. The yield strength of the steel used in the cables and hangers is 1080 MPa.

3.2 Transverse girder-support connection systems

Four transverse girder-support connection systems, illustrated in Fig. 5, are considered and compared in the present study. These include the widely used TF and TSF systems and the proposed TSD system with and without consideration of the pounding effect (TSD-P). The steel-concrete composite girder is connected to the supporting bents and towers as follows:

Case 1. **TF**: The TF system restrains the transverse and vertical translation while the longitudinal sliding movement is allowed.

Case 2. **TSF**: The TSF system restrains only the vertical translation, while both transverse and longitudinal sliding movements are allowed.

Case 3. **TSD**: The TSF system restrains the vertical translation while the TSD system, working in parallel, controls the girder-support relative displacement in the transverse direction.

Case 4. **TSD-P**: Case 3 including contact elements to consider the transverse seismic-induced pounding between the girder and the towers.

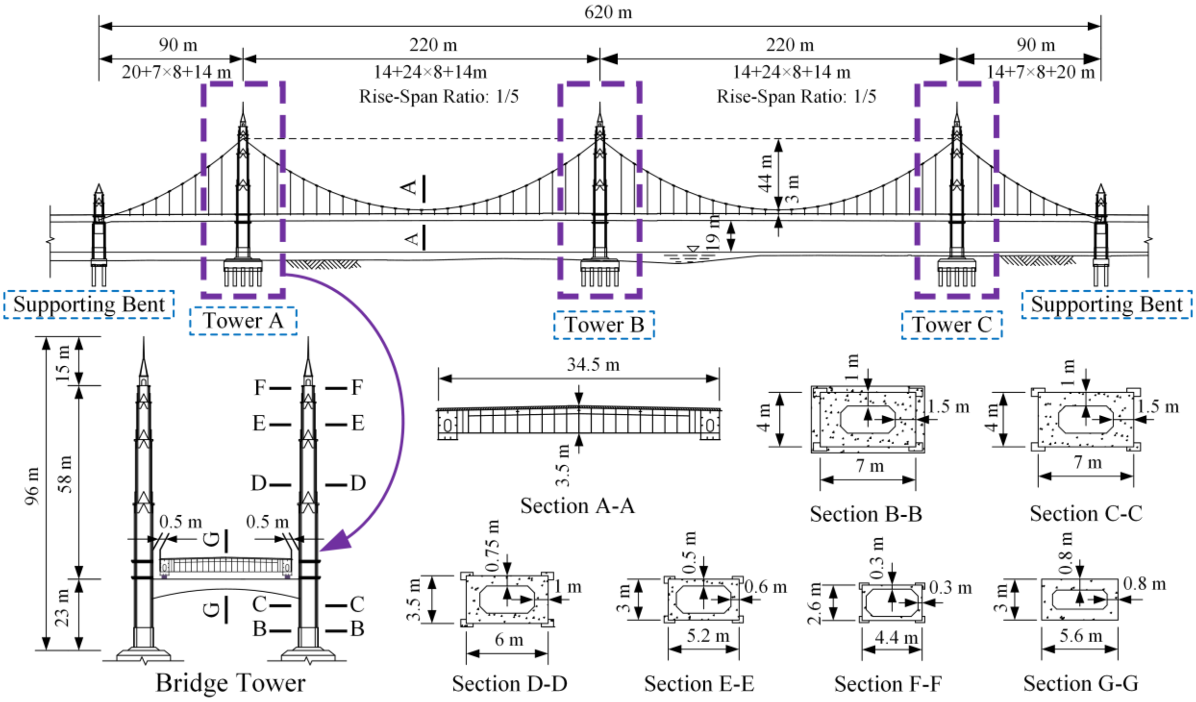

Fig. 4. Basic configurations of the prototype bridge.

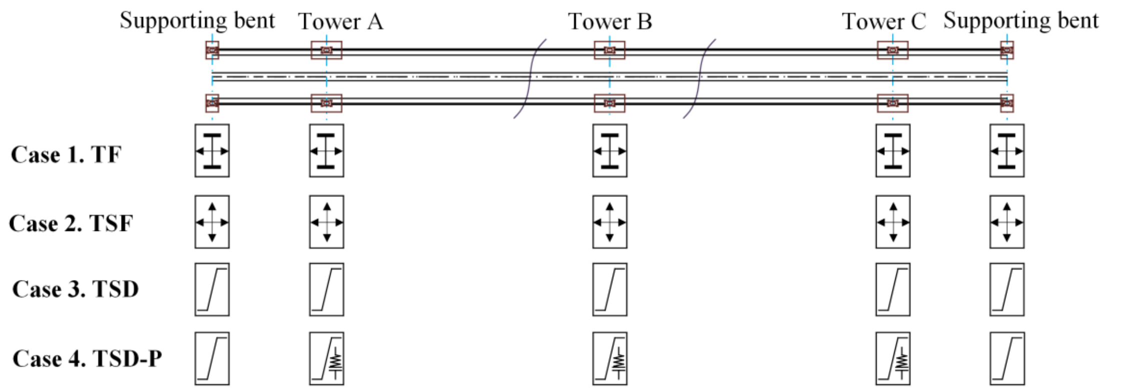

Note: "↔" denotes free sliding in the longitudinal direction; "I" denotes transverse fixed girder-support connection; "↕" denotes free sliding in the transverse direction; "∫" denotes bi-directional sliding bearing plus transverse TSD; "≢" denotes contact element; the vertical translation is restrained for four cases.

Fig. 5. Four analyzed cases of transverse girder-support connection systems.

3.3 Ground motions set

Near-fault ground motions with large velocity pulses, large permanent ground displacements, and significant vertical earthquake effects are of concern in seismic performance assessment of the long-span bridge [2,21,43]. These characteristics in near-fault ground motions make them more likely to induce the pounding phenomena compared to the cases of far-field ground motions. As a result, a total of 21 pairs of near-fault earthquake ground motions are selected from the Pacific Earthquake Engineering Research (PEER) center database for dynamic analysis in this study. Each pair of records consists of a dominant horizontal component and a corresponding vertical component. Table 1 summarizes the main information of the selected records, including moment magnitude (M_w), distance (*i.e.*, Joyner-Boore distance corresponding to the closet distance to the surface projection of an extended fault, R_{jb}), average shear wave velocity of the upper 30 m depth soil ($V_{s,30}$), horizontal peak ground acceleration (PGA-H), and vertical peak ground acceleration (PGA-V). All records are characterized by M_w between 6.53 and 7.62, R_{jb} lower than 15 km, $V_{s,30}$ ranging between 162.94 m/s and 599.64 m/s (stiff soil and very dense soil types [39-41]), PGA-H values between 0.12 g and 0.82 g, and PGA-V values between 0.08 g and 0.97 g. The considered ground motions are characterized by PGA-H/PGA-V ratios between 0.59 and 4.10, thus highlighting that for the selected near-fault ground motions, consideration of the vertical component is essential. Fig. 6 shows both the horizontal and vertical ground motions for the Cape Mendocino Earthquake of 1992 (No. 19 in Table 1). Fig. 6(a) shows the acceleration time histories, while Fig. 6(b) shows the velocity pulse of the horizontal component, characterized by a period of 4.13 s (approximately from 2 to 6 s).

Table 1 List of the selected ground motion records.

Number	Earthquake	Year	M_w	R_{jb} (km)	$V_{s,30}$ (m/s)	PGA-H (g)	PGA-V (g)	PGA-H/PGA-V
1	Imperial Valley-06	1979	6.53	8.54	208.71	0.16	0.15	1.07
2	Imperial Valley-06	1979	6.53	10.79	162.94	0.27	0.13	2.08
3	Imperial Valley-06	1979	6.53	4.90	208.91	0.37	0.29	1.28
4	Imperial Valley-06	1979	6.53	1.76	205.63	0.38	0.64	0.59
5	Landers	1992	7.28	2.19	369.00	0.73	0.82	0.89
6	Chi-Chi	1999	7.62	9.94	258.89	0.34	0.17	2.00
7	Chi-Chi	1999	7.62	9.94	258.89	0.40	0.17	2.35
8	Chi-Chi	1999	7.62	9.62	427.73	0.28	0.14	2.00
9	Chi-Chi	1999	7.62	3.76	487.27	0.28	0.18	1.56
10	Chi-Chi	1999	7.62	7.64	350.06	0.16	0.11	1.45
11	Chi-Chi	1999	7.62	5.95	454.55	0.23	0.12	1.92
12	Chi-Chi	1999	7.62	10.48	403.20	0.16	0.12	1.33
13	Chi-Chi	1999	7.62	0.89	573.02	0.33	0.23	1.43
14	Chi-Chi	1999	7.62	5.16	472.81	0.23	0.13	1.77
15	Chi-Chi	1999	7.62	6.98	538.69	0.12	0.09	1.33
16	Chi-Chi	1999	7.62	2.11	389.41	0.21	0.17	1.24
17	Chi-Chin	1999	7.62	13.13	599.64	0.14	0.09	1.56
18	Duzce	1999	7.14	12.02	293.57	0.82	0.20	4.10
19	Cape Mendocino	1992	7.01	8.49	566.42	0.18	0.08	2.25
20	Cape Mendocino	1992	7.01	8.49	566.42	0.21	0.08	2.63
21	Bam	2003	6.60	0.05	487.40	0.64	0.97	0.66

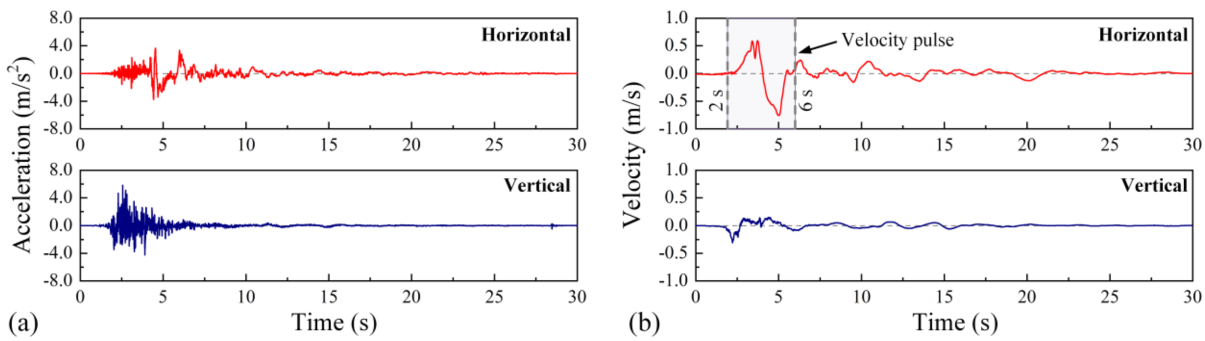

Fig. 6. Cape Mendocino records [No. 19 in Table 1]: (a) acceleration; and (b) velocity.

Figs. 7(a) and (b) show the individual and mean acceleration spectra, respectively, for the horizontal and vertical components of the selected ground motions. The ground motion pairs (*i.e.*, both horizontal and vertical) are scaled such that the PGA-H of each horizontal ground motion is equal to 1.0 g (*i.e.*, the same scaling factor is used for both horizontal and vertical components). The selected pairs of horizontal and vertical records are applied along with the transverse and vertical directions of the bridge, respectively, and the same ground motion records are imposed in all pile foundations of the bridge, *i.e.*, neglecting the spatial variability of the seismic action.

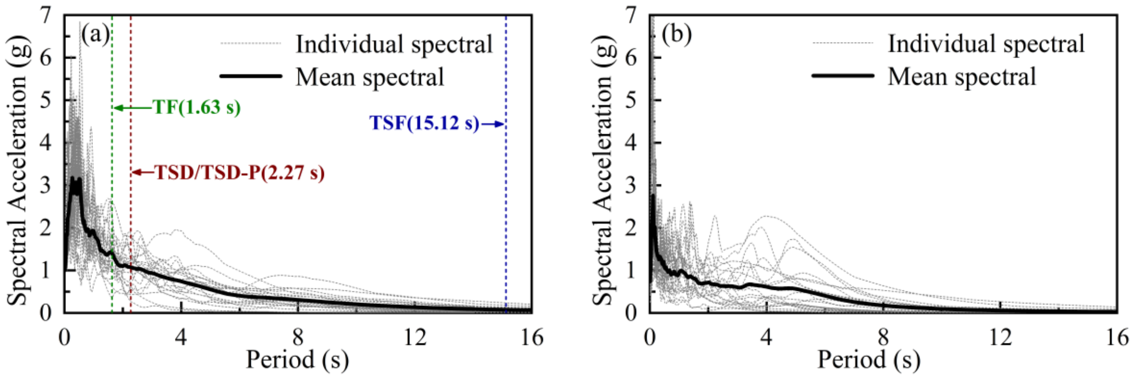

Fig. 7. Spectral acceleration of the scaled earthquake records: (a) horizontal components; and (b) vertical components.

4. Numerical analysis

4.1 Finite element model (FEM)

3D finite element models (FEM) of the case study bride considering the four aforementioned transverse girder-support connection cases are established using the SAP2000 software package [44]. Due to space constraints, only the FEM for the case with TSD-P is provided in Fig. 8. As shown in Fig. 8(a), the two main cables and the vertical hangers are modeled with truss elements merely sustaining tensile forces. The initial tensile cable force, computed under dead load, is applied to two main cables and vertical hangers to consider their contribution to the bridge geometric stiffness [29,44]. In addition, the geometrical nonlinearity of the cable elements due to the sag effect is also internally considered by using the Ernst method, *i.e.*, adopting the modified elastic modulus for main cables [45]. Bridge girders are modeled by elastic frame elements since they are not supposed to experience nonlinear deformations under the earthquake excitations. The detailed section properties of the girder are calculated from the available design information.

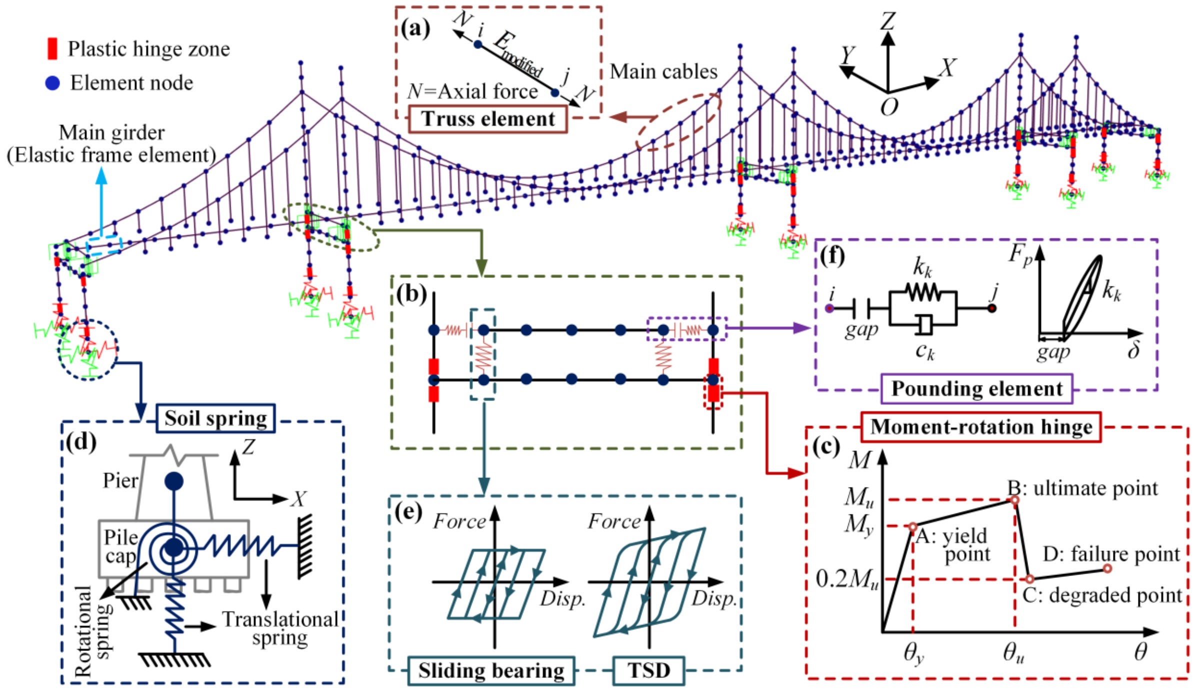

Fig. 8. Finite element model for the case of system Transverse Steel Damper with Pounding effects (TSD-P).

The towers and supporting bridge bent columns are modeled with a lumped plasticity approach by combining elastic frame elements and non-linear rotational springs to simulate the formation of plastic hinges [39,41,42]. For the case of transverse loading, due to frame action in multi-column bents, it is expected that plastic hinges are developed at the top and bottom of the tower lower segment, the bottom of the tower upper segment, and both the supporting bent column top and bottom (marked with red rectangles in the corresponding positions in Fig. 8(b)).

An idealized multi-linear model is introduced to develop the appropriate moment-rotation (M-θ) characteristics for the plastic hinges, as shown in Fig. 8(c) [46]. The values of the yield point A (θ_y, M_y) and the ultimate point B (θ_u, M_u) of the multi-linear model are determined by a cross-sectional analysis in XTRACT based on corresponding material properties. XTACT is a practical tool that can generate the sectional moment-curvature relationship or the moment-rotation capacity of plastic hinges based on a discretized layer cross-section with material nonlinearity. Fig. 9 shows the XTRACT and the idealized M-θ curves for a typical plastic hinge (*i.e.*, the supporting bent bottom). It can be found that the idealized curve with points A and B can well represent the plastic behavior of the hinge before its failure. Note that the output results for XTRACT only contain the responses that do not exceed the ultimate point B. This is because the analysis is terminated when a desired limit state has been reached within the material. Thus, according to the suggestion of Aviram *et al.* [46], for the subsequent responses the capacity of degraded point C is assumed as 0.2 times the ultimate moment (M_u), and the failure point D is set for numerical stability. The parameter values of points A, B, C, and D for the plastic hinges used in the FEM are listed in Table 2. In addition, the second-order P-Δ effects in the tower legs and bent columns are considered during the nonlinear analysis [44]. It should be noted that only considering lumped plasticity in towers and bent legs in the model may not be rigorous in an extremely seismic event because the cracking in the lower strut of towers induced by pounding could occur if the initial prestress in the strut is insufficient. Thus, in this study, the prestress of the lower strut is assumed large enough to control concrete cracking [47] and the possible decompression and cracking in the transverse strut are ignored accordingly.

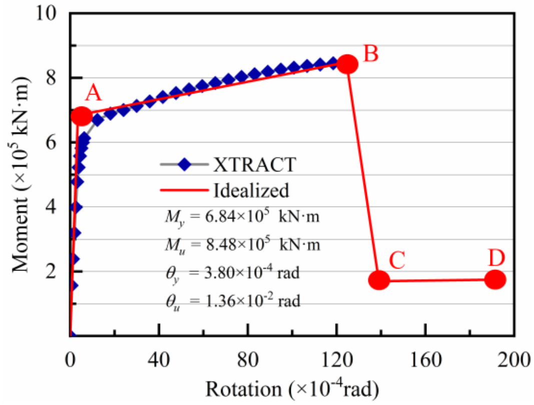

Fig. 9. Idealized moment-rotation curve before failure for the supporting bent bottom.

Table 2 Parameters of M-θ relationship for the plastic hinge model.

Tower/bent	Location	M (×10^5 kN·m)				θ (×10^{-4} rad)			
		A	B	C	D	A	B	C	D
Bent column	Top	4.5	5.7	1.1	1.1	4.1	163	165	220
	Bottom	6.8	8.5	1.7	1.7	3.8	136	138	193
Tower A and C	Bottom of upper segment	6.2	7.1	1.4	1.4	23.8	677	688	960
	Top of lower segment	6.5	7.3	1.5	1.5	4.9	25	127	182
	Bottom of lower segment	9.5	10.8	2.2	2.2	4.3	125	127	182
Tower B	Bottom of upper segment	6.1	7.0	1.4	1.4	23.7	693	704	977
	Top of lower segment	6.4	7.3	1.5	1.5	4.9	127	129	184
	Bottom of lower segment	9.4	10.8	2.2	2.2	4.3	126	128	183

Additionally, a combination of translational and rotational springs is included in the model at the pile foundation to capture the pile foundation flexibility (Fig. 8(d)) [46,48,49]. This is a simplified and approximate method for the pile foundation to represent soil-foundation interaction adopted by seismic specifications of bridges [39-42]. Based on each pile length and profiles of the surrounding soil layers, the horizontal and vertical stiffnesses of a single pile are calculated by BCAD-PILE program developed at Tongji University [50,51]. The composite behavior of the pile foundation (*i.e.*, the stiffnesses of the horizontal $k_{F,h}$ and the rotational springs $k_{F,r}$ in a pile foundation) are related to the geometry of pile groups and given as follows [48]:

$$k_{F,h} = \sum_{i=1}^{N_P} k_{h,i} \tag{6}$$

$$k_{F,r} = \sum_{i=1}^{N_P} k_{v,i} \times d_i^{\,2} \tag{7}$$

where $k_{h,i}$ and $k_{v,i}$ are the horizontal and vertical stiffnesses of the i-th pile, respectively; N_P is the number of piles for a pile foundation; and d_i is the distance between the i-th pile and the centroid of pile foundation in the direction perpendicular to the rotational axis.

4.2 Bearings and TSDs

The bearings of the TSF system are modeled by an elastic-perfectly-plastic model (Fig. 8(e)) with sliding-initiated displacement and friction coefficient set as 2 mm and 0.02, respectively [39,40]. Accordingly, the bearings of the TSF at supporting bents and towers are characterized respectively by an initial stiffness of 1000 kN/mm and 1250 kN/mm, and sliding forces of 2000 kN and 2500 kN. Conversely, the bearings of the TF system are modeled by an elastic model characterized by very high stiffness [44].

Identical TSD properties and arrangements are used for both cases of TSD and TSD-P. The TSD design is based on the methodology proposed by Zhou *et al.* [21], and the dimensions and configurations of a single set of TSD used in the case study bridge are listed in Table 3. The parameter values describing the force-displacement model of the TSD are also given in the table and are defined according to the procedure presented in Sect. 2. It is noteworthy that, to investigate the influence of the pounding effect, D_u of TSD in the current study is designed to be larger (*i.e.*, 0.55 m) than the transverse gap size (*i.e.*, 0.50 m) such that the failure of TSD is not expected before the pounding occurrence. To achieve simultaneous yielding of TSD for different supports along the girder under transverse seismic excitations, an appropriate proportionality of the number of sets for TSD among the different supports should be designed. In order to design the carrying force of TSD directly related to the inertial force of girder mass, a modal response spectrum analysis (MRSA) of the FEM of the system with the girder fully fixed to the supports (*i.e.*, TF system) is performed [23]. In this case, the ratio among the maximum transverse reaction force at supporting bent, tower A/C and tower B is 1 : 1.3 : 2.3. This proportionality is also used to design the TSDs among the different supports. Considering the available space between the girder and the tower lower strut and the minimum stiffness requirements under service loads, six, eight, and fourteen sets of TSD are installed at end supporting bents, tower A/C, and tower B, respectively. Accordingly, the numerical model of the TSD (Fig. 8(e)) at each support is represented by multiple sets of single TSD model (Table 3) combined in parallel.

Table 3 Dimensions and properties of a single set of TSD used in FEM.

t (mm)	B (m)	H (m)	n_{TP}	F_y (kN)	D_y (m)	K_1 (kN/m)	K_2 (kN/m)	D_u (m)
35.00	1.10	1.00	8	904.00	0.12	7533.33	1130.00	0.55

4.3 Pounding simulation

The Kelvin contact element is used to simulate the transverse pounding between the tower and girder (Fig. 8(f)) [29,52-54]. This element consists of a gap element and a combination of a single spring and a damper in parallel, as shown in Fig. 10(a). The element mechanism is activated when the relative transverse displacement between the tower and girder exceeds the initial separation. Thus, the force-displacement relationship of the Kelvin contact element (Fig. 10(b)) can be calculated using the following equations [29]:

$$F_p = \begin{cases} k_k(u_i - u_j - gap) + c_k(\dot{u}_i - \dot{u}_j) & u_i - u_j - gap \geq 0 \\ 0 & u_i - u_j - gap < 0 \end{cases} \tag{8}$$

where F_p is the pounding force between the i-th and j-th contact bodies; u_i and $\dot{u}_i$ are respectively the displacement and velocity of the i-th contact body; u_j and $\dot{u}_j$ are respectively the displacement and velocity of the j-th contact body; k_k and c_k are respectively the contact stiffness and damping; and *gap* denotes the gap opening between the two contact bodies.

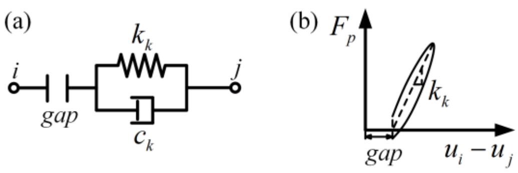

Fig. 10. Kelvin contact element: (a) schematic model; and (b) contact force-displacement relationship.

Li *et al.* [54] suggest that the contact stiffness k_k can be calculated based on the masses and the relative velocities of contact bodies according to the Hertz contact law as follows:

$$k_k = \left[\frac{(\dot{u}_i - \dot{u}_j)^2 m_i m_j}{(m_i + m_j)} \times 1.25 \right]^{0.2} \times k_h^{0.8} \tag{9}$$

where m_i and m_j are the masses of the i-th and j-th contact bodies, respectively; and k_h is the contact stiffness of the Hertz model, which can be calculated by two equivalent spheres with radii of R_i and R_j [55,56]:

$$k_h = \frac{4}{3\pi(h_i + h_j)} \left[\frac{R_i \times R_j}{(R_i + R_j)} \right]^{0.5} \tag{10}$$

in which h_i and h_j are the parameters related to contact material. The radius R of the equivalent sphere is derived from the mass m and density ρ of the corresponding contact body, and mathematically represented by [56]:

$$R = \sqrt[3]{\frac{3m}{4\pi\rho}} \tag{11}$$

Obviously, the masses of two contact bodies (*i.e.*, the contact masses of the tower leg and girder in this study) are essential for determining the contact stiffness. The contact mass of the tower leg can be estimated by using the equivalent modal method [57], by which the mass of the tower leg is equivalent to an effective modal lumped mass m_t at the level of the girder in the first mode. The effective modal mass obtained by an equivalent process is given by [29,58]:

$$m_t = \frac{\left(\sum_{j=1}^{N_m} m_j \phi_{j1} \right)^2}{\sum_{j=1}^{N_m} m_j \phi_{j1}^2} \tag{12}$$

where N_m is the number of the distributed mass points for the tower leg; m_j is the mass at the j-th distributed mass point; and ϕ_{j1} is the value of the first mode shape vector at the j-th distributed mass point. The mass of girder associated with the transverse pounding at each tower-girder location is evaluated based on the MRSA on the bridge model with the girder fully transverse-fixed to the tower supports and transverse-sliding at the ending bents [23]. The relationship among the obtained maximum transverse reaction forces of the girder at three towers is further used to calculate the corresponding girder masses that participates in transverse pounding at each tower. According to the above procedures and formulas, the contact stiffness k_k is obtained to be 9.46×10^6 kN/m for the gaps at towers A and C; and 9.68×10^6 kN/m for the gaps at the tower B.

For the contact damping parameter c_k in the Kelvin contact element, the equations proposed by Anagnostopoulos [59] are used herein:

$$c_k = 2\xi \sqrt{k_k \frac{m_i \times m_j}{m_i + m_j}} \quad \text{with} \quad \xi = \frac{-\ln e}{\sqrt{\pi^2 + (\ln e)^2}} \tag{13}$$

where ξ is the contact damping ratio involving the coefficient of restitution e. The coefficient of restitution is a parameter related to the energy losses during contact, which is typically set as 0.65 for the contact between concrete materials [60]. Consequently, the c_k values used in the Kelvin contact element at the end towers and the middle tower are determined as 4.47×10^4 and 4.65×10^4 kN·s/m, respectively. Note that the contact element and the parameter values are merely determined according to the open-published literature [52-56,59-61] and relevant mechanics concepts [56,57], and the accuracy should be validated with related experimental works. It should also be mentioned that the local damage to concrete or local buckling/fracture of reinforcement steel due to pounding (*i.e.*, resulting high-magnitude acceleration pulses and large impact forces) was neglected in the FE simulations.

Based on the established FEMs of four transverse connections, the modal analyses are carried out. The first-order transverse periods of the TF and TSF systems are 1.63 s and 15.12 s, respectively. TSD and TSD-P systems have the identical modal shape and period, both with the first-order transverse period of 2.27 s. These periods are also detailed with vertical lines in the plots of the spectrum in Fig. 7(a). The implicit Newmark direct integration method with a constant time-step of 0.005 s is used in the time-history analysis. The relatively small step-time is selected herein for detecting the impact process. In addition, Rayleigh damping with an equivalent viscous damping ratio ξ = 2% [39] is employed for all analysis cases.

5. Results and discussion

5.1 Incremental Dynamic Analyses (IDAs)

Non-linear time-history analyses are performed in an IDA [62] fashion to evaluate the seismic response of each configuration. The averaged IDA curves of the key EDPs of the four transverse girder-support connection systems are discussed in this Section. Due to symmetry conditions, only the results of the left half structure are discussed here.

Fig. 11 provides the lateral girder-support relative displacement of different transverse connection systems. Note that the relative displacement profiles of TF are always zero during the analysis. Fig. 11 shows that, due to the release of constraint, the lateral girder-support relative displacement of the TSF system increases almost linearly as the PGA-H (referred to as PGA in the following analysis and plots) increases. In this case, the critical relative displacement of 0.5 m (*i.e.*, pounding onset) occurs at all towers and bent supports with a PGA corresponding to 0.1g. This phenomenon is prevented by the introduction of the TSD in the transverse girder-support connection, *i.e.*, the case of the TSD system. In comparison with TSF, the relative displacement at the supports of TSD is significantly reduced to approximately 0.05 m for PGA of 0.1g. With the increase of the seismic intensity level, the TSDs at the bent, tower A, and tower B yield at 0.21, 0.18, and 0.17 g, respectively (*i.e.*, vertical black dotted line in Fig. 11). It is noteworthy that the occurrence of yielding at the three support locations is relatively close, which meets the design principle of simultaneous yielding for the TSDs at different supports. For a PGA of 0.45 g, the TSD at tower B first reaches its ultimate displacement capacity of 0.55 m (*i.e.*, vertical red dotted line in Fig. 11). Successively, the failure of TSD at tower A and at the end supporting bent occur at 0.54g and 0.63g, respectively. This indicates that the girder-support location at tower B is more susceptible to damage for the TSD system of the case-study bridge. However, it is worth mentioning that beyond the first TSD failure, the IDA curves are not accurate because the TSD model cannot capture its ‘real’ response at failure. Note that the low cycle fatigue of TSD is not considered in this study because TSD has been experimentally validated to possess a superior fatigue performance [22].

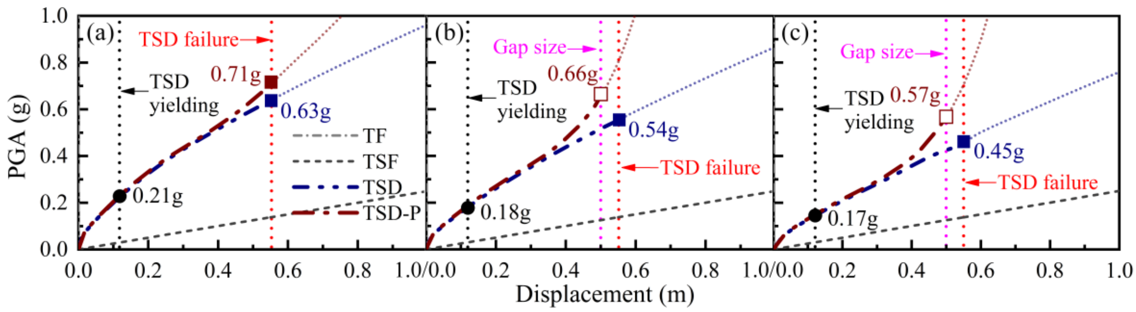

Fig. 11. Comparison of the mean girder-support relative transverse displacement at: (a) supporting bent; (b) tower A; and (c) tower B.

The inclusion of potential pounding between the girder and tower leg reproduces a more realistic transverse seismic response for the TSD system (*i.e.*, TSD-P). For PGA values smaller than 0.3 g, no noticeable difference is observed between the IDA curves of TSD and TSD-P systems since only a few pounding events occur; thus, the yielding of TSD at these two systems also coincides. Fig. 12 shows the force-displacement hysteretic behavior of TSDs in two TSD systems under No. 19 ground motion record (Cape Mendocino 1992) with PGA = 0.2 g. The force-displacement histories of the TSDs in two systems are identical, both experiencing nonlinearity. However, for PGA values exceeding 0.3 g, the initial gap cannot accommodate the girder-support relative displacement, and the influence of pounding becomes more pronounced. It can be observed that, as a result of pounding, the relative

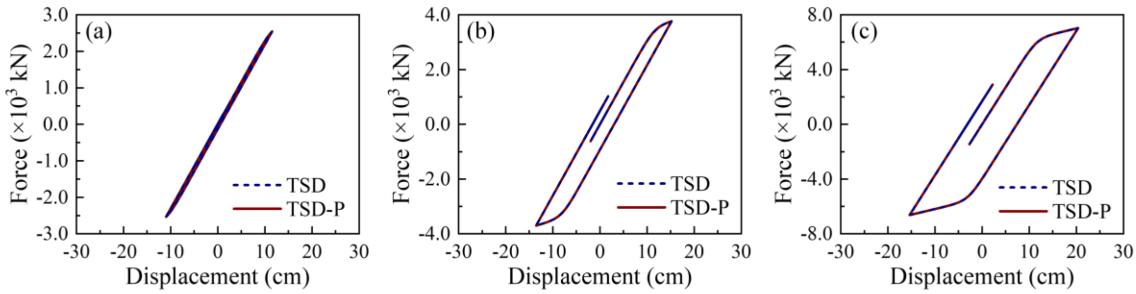

Fig. 12. Force-displacement relationship of TSDs under the No.19 ground motion with PGA = 0.2 g: (a) supporting bent; (b) tower A; and (c) tower B.

transverse displacement diminishes for all towers (Figs. 11(b) and (c)), and the failure of TSD does not occur as expected from the design. In addition, it is worth mentioning that, despite the pounding model has been defined to capture the interaction of the two bodies at contact, the lack of a specific validation does not ensure the validity of the results for relative displacements larger than the gap size (*i.e.*, vertical pink dotted line in Fig. 11(b) and (c)). The TSD of towers A and B in the TSD-P system reach the gap size at PGA values equal to 0.66 and 0.57 g, respectively, corresponding to the 22% and 27% increase with respect to the TSD failure in the TSD system. Besides, although the pounding phenomenon is not considered at the bent supports for the TSD-P system, the relative displacement at this location is also similarly restricted by the pounding occurring at the towers.

To enable a more straightforward interpretation of the pounding effect on the girder-support relative displacement, the time history results at the tower B under No. 19 ground motion record with two intensity levels are plotted in Fig. 13. As expected, the relative displacement response in TSD-P is aligned well with that in TSD for the case with PGA = 0.2 g (Fig. 13(a)) since no pounding effects are observed, *i.e.*, gaps between the girder and tower legs provide sufficient space for the girder transverse motion (the maximum girder-support relative displacement of 20.1 cm). However, as shown in Fig. 13(b), with a PGA value equal to 0.7 g, the pounding effect becomes evident, and the relative displacement in TSD-P is almost restricted within the gap size (*i.e.*, 50 cm) during the entire time history of the selected seismic input, due to the two collisions, occurring at times 3.58 s and 5.02 s, respectively. The opposite signs of displacement for two collisions indicate that they occur at left and right tower legs, respectively. When the pounding phenomenon is precluded in the time history analysis (*i.e.*, TSD case), the displacement response significantly increases to unrealistic values larger than 100 cm.

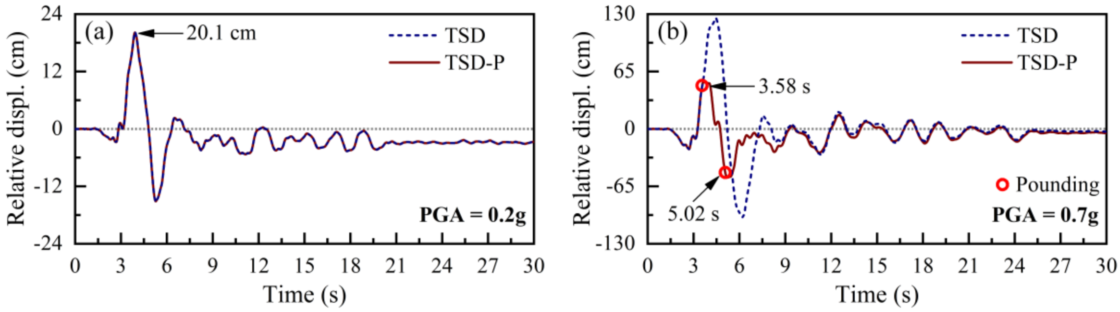

Fig. 13. Transverse relative displacement response of the girder-support at the tower B under the No. 19 ground motion with: (a) PGA = 0.2 g; and (b) PGA = 0.7 g.

In light of the previous discussion, the bottom section of the upper segment of the tower leg (Section H-H in Fig. 14) is of great concern due to the occurrence of pounding that can increase the seismic demand at this location. Fig. 14 compares the curvature ductility demands of the tower at Section H-H among the different systems at various PGA levels. It is observed that TF and the TSF systems exhibit the largest curvature ductility demand. In the TF system, this is due to the high seismic demand related to the short vibration period (Fig. 7(a)). Conversely, in the TSF system, this is related to the inertia forces of the girder that are transmitted through the vertical hangers and main cables to the tower top under the seismic excitations, hence contributing to the substantial deformations of the upper tower leg due to the long lever arm. Thus, Section H-H of the towers in both these conventional transverse systems yields for relatively small PGA values (*i.e.*, about 0.3 g). A reasonable balance between the internal force and deformation of the tower legs is maintained using TSD in the transverse direction. As shown in Figs. 14(a) and (b), the yielding of Section H-H in TSD occurs at approximately 0.50 g, which is 67% greater than that in TF and TSF. It is also noteworthy that for the TSD system, the pounding effect for the tower Section H-H cannot be neglected when PGA is larger than 0.5 g. Despite the pounding phenomenon is detected in a few cases also for PGA values equal to 0.3 g (Fig. 11), this does not significantly affect the curvature ductility demands of the upper tower leg at Section H-H until the yielding of section curvature. After yielding, the pounding

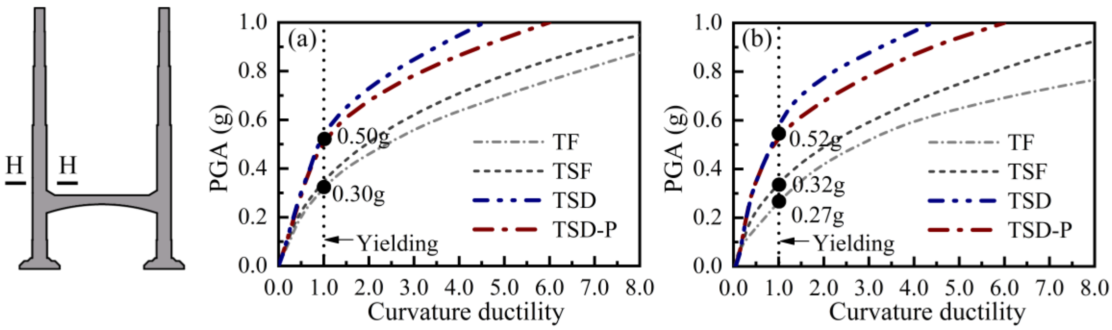

Fig. 14. Comparison of the curvature ductility at the tower Section H-H: (a) tower A; and (b) tower B.

In addition, the seismic-induced pounding has the potential disadvantage of amplifying the shear force of the tower Section H-H. Fig. 15 illustrates the IDA curves of the shear force demands at this location for towers A and B. The shear force of the tower is related to the force from the cables, the higher mode effects of the tower itself, and the pounding effect when considered. For TSF, Section H-H suffers from the relatively large seismic shear force as the cables sustain the whole inertial force of the girder. The shear force in TF is minimal because the main girder is rigidly connected to the transverse lower strut, and thus most of the inertial force of the main girder is directly transmitted to the tower base through the lower strut. The figures also illustrate that the use of TSD generates shear demand values at Section H-H that are approximately in between these two conventional transverse systems. It is worth mentioning that the pounding results in a sharp increase of the shear force in the TSD-P, and even sectional shear failure under extreme earthquake excitations (0.89 g and 0.80 g for tower A and tower B, respectively). Fig. 16 shows the time history of the collision force at the left and middle towers under the No. 19 earthquake. It can be found that the collisions between the tower legs and girder induces a large pounding force, which is comparable to the shear resistance of the tower leg. Thus, for the pounding-prone structures, such as the suspension bridge with a transverse TSD system, the impact load should be included in the seismic analysis or design process to prevent the shear failure of the towers.

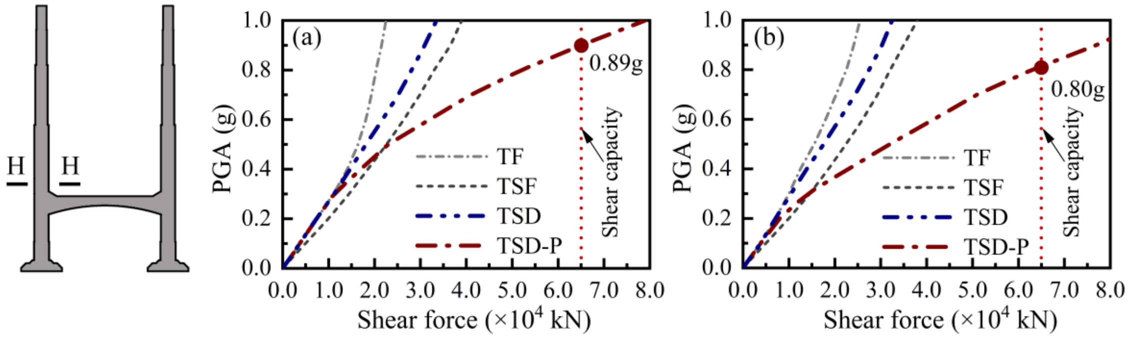

Fig. 15. Comparison of the shear force at the tower section H-H: (a) tower A; and (b) tower B.

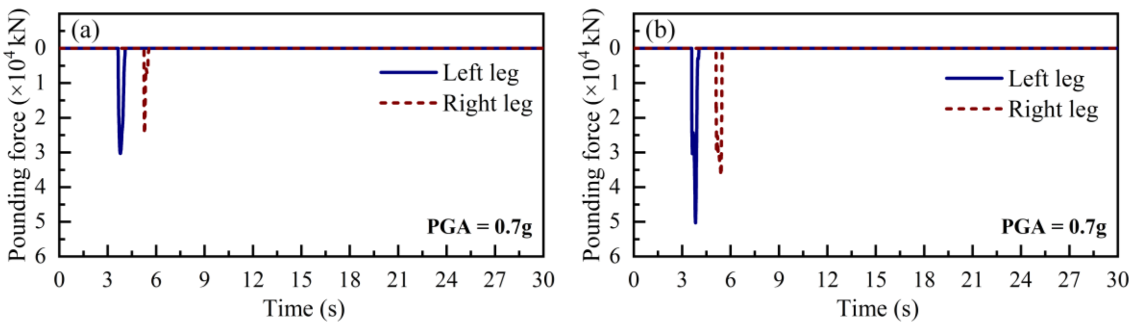

Fig. 16. Pounding force time-history at the tower section H-H under the No.19 ground motion with the PGA = 0.7 g: (a) Tower A; (b) Tower B.

5.2 Comparative fragility analysis

Fragility curves provide the probability of exceeding a specified limit state or failure condition, conditional to the strong-motion shaking severity, quantified by means of an appropriately selected IM [33]. In the present paper, they are used to provide a better interpretation of the advantages of utilizing TSD for controlling transverse response and the importance of considering pounding also accounting for the ground motion uncertainties. Based on the results of IDAs, the damage probability of a structure component at a given IM level, P_f, is numerically calculated as:

$$P_f = [EDP \geq DS \mid IM] = \frac{n}{N} \tag{14}$$

where n is the number of cases with the EDPs exceeding the threshold of each damage state (DS) for the given value of IM; and N is the total number of analysis cases. The numerical curve is successively regressed by a lognormal function by using the Maximum Likelihood Method suggested by Baker [63]. Bridge towers are the components directly sustaining the pounding force; thus, the curvature ductility of tower base μ_ϕ and the drift ratio of tower θ_d (defined as the top displacement divided by tower height) are selected as the EDPs of interest for the fragility analysis. The DS thresholds for these two EDPs at four DSs (*i.e.*, slight, moderate, extensive, and collapse recommended by HAZUS [64]) are listed in Table 4.

Table 4 Definition of the tower damage indexes and corresponding DS thresholds.

Damage Index	slight	moderate	extensive	collapse
μ_ϕ [65]	$\mu_\phi > 1$	$\mu_\phi > 2$	$\mu_\phi > 4$	$\mu_\phi > 7$
θ_d [66]	$\theta_d > 0.007$	$\theta_d > 0.015$	$\theta_d > 0.025$	$\theta_d > 0.050$

Note: μ_ϕ refers to the sectional curvature ductility; θ_d refers to the drift ratio of the tower.

Fig. 17 shows the fragility curves of the four investigated transverse systems in terms of the sectional curvature ductility at the base of tower B. As expected, the results show that using the TSD system allows a reduction of the fragility at all DSs compared to the TF and TSF systems. For example, for the moderate DS, the TF and TSF show the probability of failure that is respectively about four and two times the one in TSD. Nevertheless, this large difference is significantly reduced when the pounding effects are considered (TSD-P). This is related to the shear force increase in tower legs as a consequence of the pounding (Fig. 15), which inevitably results in the larger bending moment and corresponding curvature at the tower base.

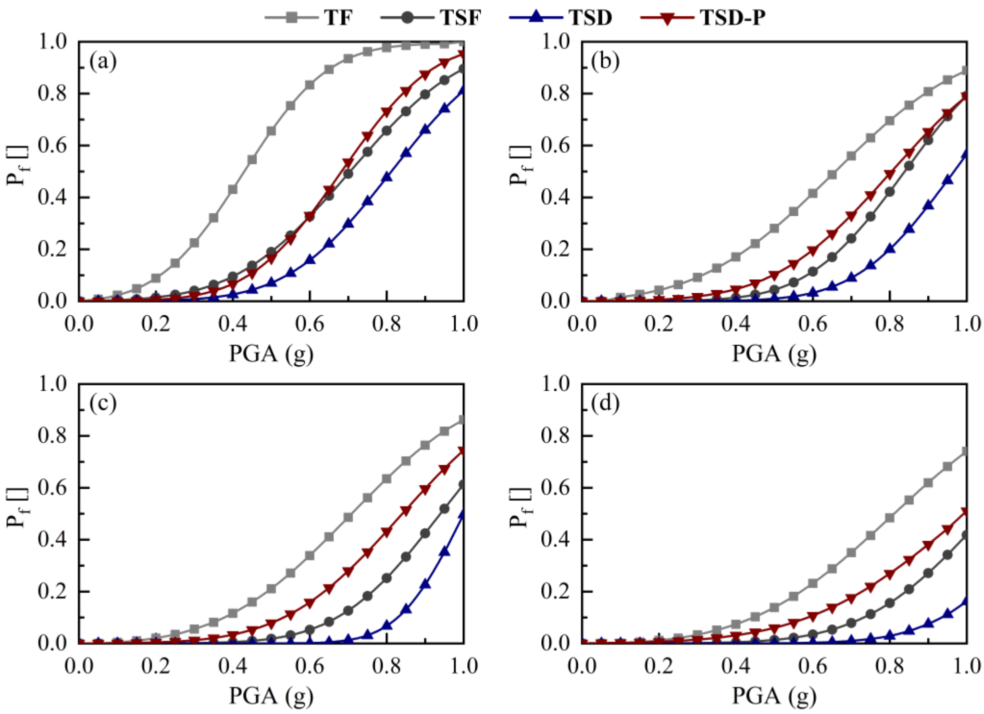

Fig. 17. Fragility curves of the curvature ductility μ_ϕ of tower B for different transverse systems at four specified damage states: (a) slight; (b) moderate; (c) extensive; and (d) complete.

Fig. 18 shows the fragility curves of the four investigated transverse systems in terms of the tower top drift ratio. The results show that, the use of the TSD decreases the probability of failure measured in terms of tower top drift ratio. For example, also in this case, for the moderate DS, the TF and TSF show the probability of failure that is significantly higher than the one in TSD. It is noteworthy that the fragility curves of cases TSD and TSD-P are almost identical, implying that the influence of pounding on the tower top drift ratio for TSD is very limited This is because the tower legs are almost cantilever structures whose responses are controlled by multiple modes. The high modes of this structure contribute more significantly to the force than to the displacement according to the modal combination analysis results estimated by Chopra [57], thus minimizing the pounding effects on the displacement response at the tower top.

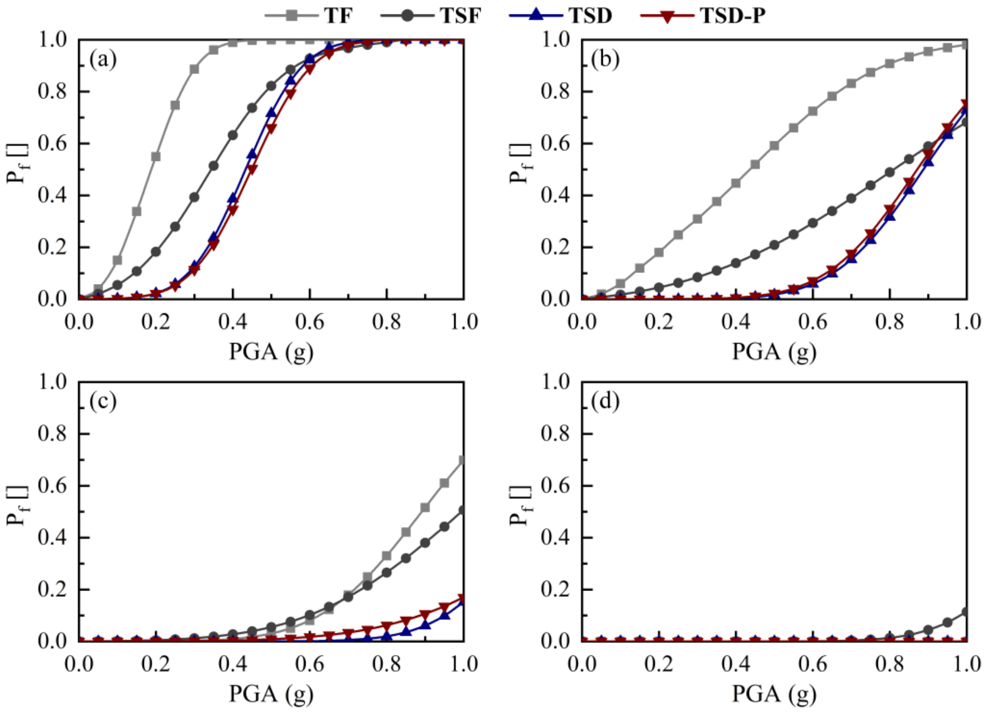

Fig 18. Fragility curves of the drift ratio θ_d of tower B for different transverse systems at four specified damage states: (a) slight; (b) moderate; (c) extensive; and (d) complete.

5.3 Energy-based analysis of TSD systems

The energy-based analysis is carried out to gain insight into the mechanism of pounding effects in TSD systems. During a seismic excitation, the energy equation for seismic analysis can be obtained by integrating both sides of the equation of motion from the initial state to the end of the dynamic response as follows [29,57]:

$$\underbrace{\int\{\dot{x}\}^T[M]\{\ddot{x}\}dt}_{E_K}+\underbrace{\int\{\dot{x}\}^T[C]\{\dot{x}\}dt}_{E_D}+\underbrace{\int\{\dot{x}\}^T\{f(t)\}dt}_{E_E+E_P}+\underbrace{\int\{\dot{x}\}^T\{f_P(t)\}dt}_{E_{Po}}=\underbrace{-\int\{\dot{x}\}^T[M][r]\{a_g(t)\}dt}_{E_I} \tag{15}$$

where $[M]$ and $[C]$ represent the mass and viscous damping matrix, respectively; $\{f(t)\}$ is the nonlinear restoring force vector at time t; $\{f_P(t)\}$ is the pounding force vector at time t; $[r]$ is a matrix related to the ground motion input components and the degree of freedom; $\{\ddot{x}\}$ and $\{\dot{x}\}$ are respectively the acceleration and velocity vectors relative to the ground; and $\{a_g\}$ is the ground acceleration. The six energy components E_K, E_D, $E_E + E_P$, E_{Po}, and E_I at the bottom side of Equation (15) are respectively: *1)* the structural kinetic energy associated with the motion (E_K); *2)* the energy dissipated by global damping (E_D), *i.e.*, stiffness- and mass-proportional damping; *3)* the sum of elastic strain energy (E_E) and plastic deformation energy (E_P, *i.e.*, energy dissipated through the hysteretic response of TSDs and plastic frame hinges.); *4)* the energy dissipated by pounding (E_{Po}); and *5)* the total input energy (E_I).

Fig. 19 shows the energy time history of the input energy (E_I) and the dissipated energy ($E_D + E_P$) of two TSD systems (TSD and TSD-P) under the No.19 ground motion record with the PGA = 0.7 g. It is noteworthy that Fig. 19(b) also shows the energy dissipated due to pounding (E_{Po}) for the TSD-P case. In both TSD systems, a significant increase of input energy occurs in the interval 2-6 s, which coincides with the onset and duration of the velocity pulse of the ground motion (Fig. 6(b)). This finding indicates that most of the energy of the No.19 ground motion is supplied by its velocity pulse, which is in agreement with the results of Sharbati *et al.* [67] The E_I values of the TSD and TSD-P systems are 4.47×10^5 and 3.89×10^5 kJ, respectively, with a percentage difference of 13.0%. The lower seismic input energy in the TSD-P system can be explained by the difference in structural dynamic properties because the input seismic energy is primarily governed by the respective earthquake accelerogram and structural dynamic characteristics according to the previous studies [68,69]. For the TSD-P, the pounding between the girder and towers results in a severe nonlinear response of the towers (as shown in Fig. 14), hence, significantly modifying its structural dynamic properties with respect to the TSD. Among others, one significant difference in the dynamic response is the structural period elongation. Additionally, as shown in Fig. 19(b), the increase of E_{Po} in TSD-P merely occurs at two time-points (3.58 and 5.02 s, Fig. 13(b)), which produces the negligible energy of 1.26×10^3 kJ. This is because the contact duration is relatively short, resulting in that the energy is not significant.

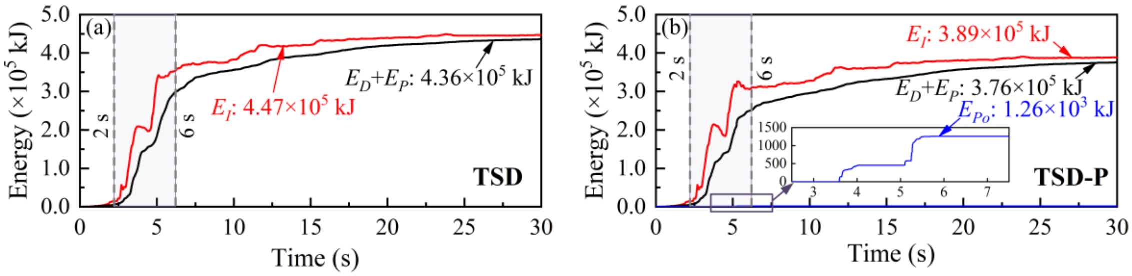

Fig. 19. Time history of total input energy (E_I) and energy dissipated by global damping (E_D), yielding (E_P), and pounding (E_{Po}) when subject to No.19 ground motion (PGA = 0.7 g): (a) TSD; and (b) TSD-P.

Fig. 20 shows the time history of two conservative types of energy (kinetic energy E_K and elastic strain energy E_E) for TSD and TSD-P systems. Both types of energy in the structures gradually decline because the elastic strain can be recovered and the motion of the structure decays [44,57]. During the vibration phase, a peak of E_K, with the energy of 9.98×10^4 kJ, is observed in the TSD system (Fig. 20(a)), whereas the E_E is relatively smaller (6.96×10^4 kJ). A possible reason is that in comparison with the deformation of structural members, the seismically induced transverse girder motion in long span suspension bridges also considerably increases although the TSDs are employed in it. However, the pounding effect significantly modifies the subsequent states of the motion and the corresponding energy distribution when it is considered. Fig. 20(b) shows a higher value of E_E (9.36×10^4 kJ) in the TSD-P system and a lower value of E_K (6.83×10^4 kJ) with respect to the TSD case. By comparing two TSD systems, it can be observed that the process of energy conversion between E_E and E_K occurs at the time of the two impacts, accompanied by the reduced E_K at the expense of the increase of E_E. The E_E is related to the seismic forces and stresses to be designed against; thus, this observation is yet another indication of the increased strength and ductile design demands in the TSD system due to pounding.

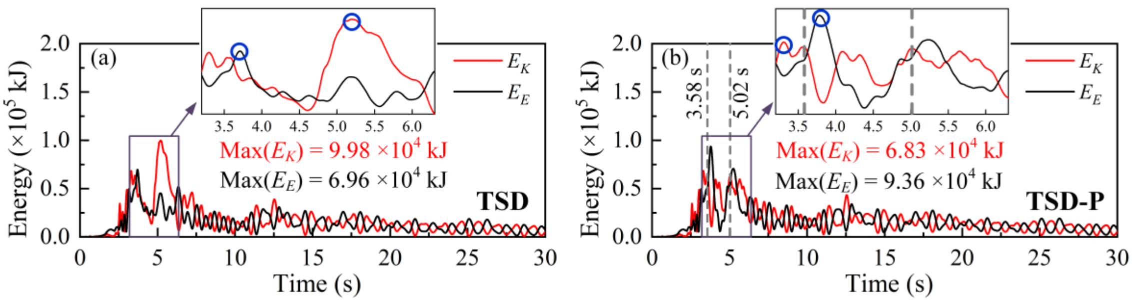

Fig. 20. Time history of structural kinetic energy (E_K) and elastic strain energy (E_E) when subjected to No.19 ground motion (PGA = 0.7 g): (a) TSD; and (b) TSD-P.

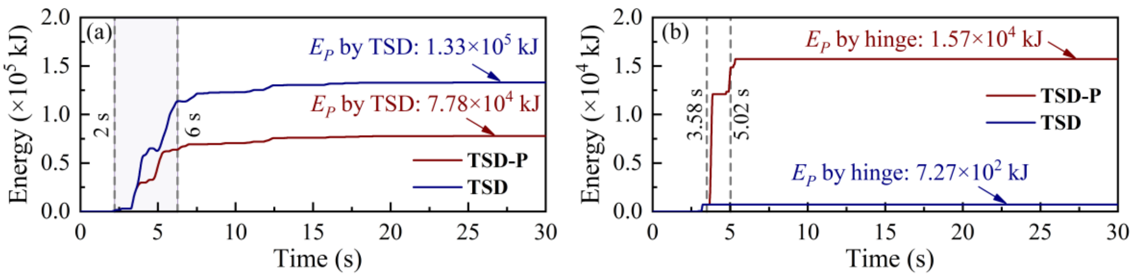

Fig. 21. Time history of the plastic deformation energy (E_P) in the TSD and TSD-P systems when subjected to No.19 ground motion (PGA = 0.7 g): (a) by TSD; and (b) by plastic frame hinge.

The transverse pounding also affects the plastic deformation energy E_P, as shown in Fig. 21. The TSDs and the frame plastic hinges are two main sources of E_P in this study and are individually evaluated and displayed in the figure. Fig. 21(a) shows that with a similar trend like that of the ground input energy E_I, the energy dissipated by TSD significantly increases within the time range 2-6 s due to the velocity pulse, no matter whether the pounding phenomenon is excluded or included. However, TSD's dissipation energy in the TSD-P system (7.78×10^4 kJ) is lower than that in the TSD system because of the restriction of excursions in TSDs. This restriction effect of pounding generates a reduction of total TSD dissipation energy of 41% compared to that in the TSD system. On the other hand, the pounding phenomenon results in adverse effects for the dissipation energy of frame hinges, as shown in Fig. 21(b). Two contacts induce the large inelastic excursions of the towers, which provides energy dissipation through the yielding mechanism of the plastic hinges, thus introducing nonlinearity and corresponding damage in the TSD-P system. For the selected ground motion case, the maximum energy dissipated by the nonlinearity of the towers after pounding is equal to 1.57×10^4 kJ, which is significantly larger than that in TSD.

The preceding energy analysis indicates that although the input seismic energy between two TSD systems has a slight difference, the proportion of various kinds of energy in them is diverse due to the transverse pounding between the girder and towers. In fact, based on the energy analysis results, for the long-span suspension bridges with TSDs, more attention should be directed to the tower transverse responses rather than the girder because of the restriction effects of pounding on both sides of the girder.

6. Conclusion

The present paper investigates the effectiveness of the transverse steel damper (TSD) system in balancing the seismic transverse displacement and the inertial force responses for long-span suspension bridges. Numerical simulations are performed using a detailed 3D model of a case study bridge where the TSD hysteretic behavior is implemented through a validated Bouc-Wen model. Potential transverse pounding between the girder and bridge towers is also included in the analysis for a realistic seismic response scenario. The transverse seismic response of the case study bridge with the TSD system is compared with two common transverse girder-support systems [*i.e.*, transverse fixed (TF) and transverse sliding-free (TSF)] based on Incremental Dynamic Analysis (IDA) and fragility curve. Additional considerations are successively made on the pounding effects of the system under large earthquakes based on an energy point of view. The following main outcomes can be drawn:

1. In comparison with the TF or TSF girder-support connection, the use of TSDs between the girder and tower struts is an effective option for achieving a relative balance between the transverse girder displacement or tower deformation and the inertial force of the towers. The use of the TSD shows a significant reduction of the probability of failure in terms of the tower drift and sectional curvature. For example, considering a moderate damage state, a reduction of the exceedance probability for the tower sectional curvature in TSD is around 75% and 50% compared to TF and TSF, respectively.
2. The use of TSD system represents an effective strategy in controlling the relative transverse displacement between the girder and tower legs in the suspension bridge, which implies that it could be a retrofitting solution for the existing suspension bridges with the issues of transverse constraint degradation. However, pounding effects can still be observed at this location under seismic actions characterized by large intensities or by velocity pulses.
3. The transverse pounding between the girder and tower legs increases the tower shear force and sectional curvature demands with a consequent higher vulnerability to the failure of the tower. However, the detrimental effect of pounding on the tower top displacement is not pronounced.
4. The transverse pounding between the girder and tower legs results in a significant variation of the energy balance due to the change of the dynamic properties of the structure. In general, the structural elastic strain energy and the plastic deformation energy of the towers are increased.
5. The current study neglects the local damage in the form of material failure cracking/crushing of the concrete or local damage of reinforcement steel of the RC member due to stress concentration at the time of collisions. In addition, the transverse deck-towers pounding analysis in this study is based on a specific suspension bridge; however, the pounding effects are affected by many factors, such as contact model parameters and spatial variability of the ground record. Thus, additional study of complex conditions and more bridge layouts or sensitivity analysis on a certain factor are required, aiming to provide detailed and general design recommendations for TSD-P system.
6. There are no standard modelling procedures that can reliably simulate pounding effects and there is a significant need for large-scale experimental tests that would allow the calibration/validation of advanced models accounting for the pounding model and relevant parameters.

7. Acknowledgements

The authors appreciate the financial support provided by the National Natural Science Foundation of China (Grant NO.51838010) and the China Scholarship Council (Grant No.202006260245 and No.202006260048). The authors also sincerely thank to Prof. Aijun Ye and PhD student Lianxu Zhou of Tongji University for their assistance in this study.

Reference

[1] Sun L, Xie W. Evaluation of pile-soil-structure interaction effects on the seismic responses of a super long-span cable-stayed bridge in the transverse direction: A shaking table investigation. Soil Dyn Earthq Eng 2019;125:105755.

[2] Guan Z, You H, Li J. An effective lateral earthquake-resisting system for long-span cable-stayed bridges against near-fault earthquakes. Eng Struct 2019;196:109345.

[3] Shen X, Wang X, Ye Q, Ye A. Seismic performance of transverse steel damper seismic system for long span bridges. Eng Struct 2017;141:14-28.

[4] Chadwell C. Near-source earthquake on the Ji-Lu cable-stayed bridge in the 21 September 1999 Chi-Chi Taiwan Earthquake. Phd. Dissertation, Berkeley. 2001.

[5] Chang KC, Mo YL, Chen CC, Lai LC, Chou CC. Lessons learned from the damaged Chi-Lu cable-stayed bridge. J Bridge Eng 2004;9(4):343-52.

[6] Tsopelas P, Constantinou MC, Kim YS, Okamoto S. Experimental study of FPS system in bridge seismic isolation. Earthq Eng Struct Dyn 1996;25(1):65-78.

[7] Mosqueda G, Whittaker AS, Fenves GL. Characterization and modeling of friction pendulum bearings subjected to multiple components of excitation. J Struct Eng 2004; 130(3):433-42.

[8] Pecker A. Design and construction of the Rion Antirion Bridge. Geotechnical Engineering for Transportation Projects 2004:216-40.

[9] Yan B, Du XL, Han Q. Application of hybrid seismic mitigation and isolation device to seismic design of single-pylon cable-stayed bridge. Bridge Const 2014;44(6):101-06. (in Chinsese)

[10] Kelly JM, Skinner RI, Heine AJ. Mechanisms of energy absorption in special devices for use in earthquake resistant structures. Bulletin of the New Zealand Society for Earthquake Engineering 1972;5(3):63-88.

[11] Parducci A, Mezzi M. Seismic isolation of bridges in Italy. Bulletin of the New Zealand Society for Earthquake Engineering 1992;25(3):193-202.

[12] Martínez-Rodrigo MD, Lavado J, Museros P. Dynamic performance of existing high-speed railway bridges under resonant conditions retrofitted with fluid viscous dampers. Eng Struct 2010;32(3):808-28.

[13] Zhou P, Liu M, Li H, Song G. Experimental investigations on seismic control of cable-stayed bridges using shape memory alloy self-centering dampers. Struct Control Health Monit 2018;25(7):e2180.

[14] Tsai KC, Chen HW, Hong CP, Su YF. Design of steel triangular plate energy absorbers for seismic-resistant construction. Earthq Spectra 1993;9(3):505-28.

[15] Parulekar YM, Reddy GR, Vaze KK, Ghosh AK, Kushwaha HS and Babu RR. Seismic response analysis of RCC structure with yielding dampers using linearization techniques. Nucl Eng Des 2009;239(12):3054-61.

[16] Camara A. Seismic behaviour of cable-stayed bridges: design, analysis and seismic devices. Universidad Politécnica de Madrid-PhD Thesis; 2011.

[17] Camara A, Astiz MA. Analysis and control of cable-stayed bridges subject to seismic action. Struct Eng Int 2014;24(1): 27-36.

[18] Infanti S, Papanikolas P, Benzoni G, Castellano MG. Rion-Antirion Bridge: Design and full-scale testing of the seismic protection devices. In Proceedings of the 13th world conference on earthquake engineering 2004:2174-89.

[19] Combault J. The Rion-Antirion bridge - when a dream becomes reality. Front Architect Civ Eng China 2011;5(4):415-26.

[20] Shen X, Camara A, Ye A. Effects of seismic devices on transverse responses of piers in the Sutong Bridge. Earthq Eng Eng Vib 2015;14(4):611-23.

[21] Zhou L, Wang X, Ye A. Shake table test on transverse steel damper seismic system for long span cable-stayed bridges. Eng Struct 2019;179:106-19.

[22] Zhou L, Wang X, Ye A. Low cycle fatigue performance investigation on transverse steel dampers for bridges under ground motion sequences using shake-table tests. Eng Struct 2019;196:109328.

[23] Camara A, Cristantielli R, Astiz MA, Málaga-Chuquitaype C. Design of hysteretic dampers with optimal ductility for the transverse seismic control of cable-stayed bridges. Earthq Eng Struct Dyn 2017;46(11):1811-33.

[24] Chouw N, Hao H. Pounding damage to buildings and bridges in the 22 February 2011 Christchurch earthquake. Int J Prot Struct 2012;3(2):123-39.

[25] Yen WP, Chen G, Yashinski M, et al. Lessons in bridge damage learned from the Wenchuan earthquake. Earthq Eng Eng Vib 2009;8(2):275-85.

[26] Tubaldi E, Freddi F, Barbato M. Probabilistic seismic demand model for pounding risk assessment. Earthq Eng Struct Dyn 2016;45(11):1743-58.

[27] Jia HY, Lan XL, Zheng SX, Li LP, Liu CQ. Assessment on required separation length between adjacent bridge segments to avoid pounding. Soil Dyn Earthq Eng 2019;120:398-407.

[28] Dimitrakopoulos EG. Seismic response analysis of skew bridges with pounding deck-abutment joints. Eng

Struct 2011;33(3):813-26.
[29] Shen Y, Li Y, Xu W, Li J. Evaluation of seismic-induced impact interaction between a cable-stayed bridge and its approach spans using a simplified analysis model. J Earthq Eng 2020;14:1-21.
[30] Deng YL, He XJ. Effect of pounding at expansion joints on seismic response of long-span suspension bridge under strong earthquake. Adv Mat Res 2011;163-167:4373-77.
[31] Takeda T, Mizutani T, Nagayama T, Fujino Y. Reproduction of cable-stayed bridge seismic responses involving tower-girder pounding and damage process estimation for large earthquakes. J Bridge Eng 2019;24(2):04018112.
[32] Freddi F, Padgett JE, Dall'Asta A. Probabilistic seismic demand modeling of local level response parameters of an RC frame. Bull Earthq Eng 2017;15(1):1-23.
[33] Gutiérrez-Urzúa LF, Freddi F, Sarno LD. Comparative analysis of code based approaches for the seismic assessment of existing steel moment resisting frames. J Constr Steel Res 2021;181:106589.
[34] Cao Z, Wang Z, Du P, Liu H, Fan F. Quasi-static experiments on steel plate shear walls reinforced with X-shaped restrainers. J Build Eng 2020;31:101451.
[35] Freddi F, Ghosh J, Kotoky N, Raghunandan M. Device uncertainty propagation in low-ductility RC frames retrofitted with BRBs for seismic risk mitigation. Earthq Eng Struct Dyn 2021;50(9):2488-509.
[36] Freddi F, Tubaldi E, Zona A, Dall'Asta A. Seismic performance of dual systems coupling moment-resisting and buckling-restrained braced frames. Earthq Eng Struct Dyn 2021;50(2):329-53.
[37] Wen YK. Method for random vibration of hysteretic systems. J Eng Mech 1976;102 (2):249-63.
[38] Liu T,Shen X, Ye A. Hysteretic model parameter of the steel triangular plate damper in bridges. Struct Eng 2014;30(6):54-60. (in Chinsese)
[39] MOHURD. Code for seismic design of urban bridge (CJJ 166-2011). Beijing: China Architecture and Building Press; 2011. (in Chinsese)
[40] MOT. Guidelines for seismic design of highway bridges (JTG/T B02-01-2008). Beijing: China Communications Press; 2008. (in Chinsese)
[41] AASHTO. AASHTO guide specifications for LRFD seismic bridge design. Washington, DC: American Association of State Highway Transport Officials; 2015.
[42] BSI. Eurocode 8: Design of structures for earthquake resistance - Part 2: Bridges. European Committee for Standardization; 2011.
[43] Li S, Dezfuli FH, Wang J, Alam MS. Longitudinal seismic response control of long-span cable-stayed bridges using shape memory alloy wire-based lead rubber bearings under near-fault records. J Intel Mat Syst Str 2018;29(5):703-28.
[44] CSI analysis reference manual for SAP2000. Computers and Structures, Inc. Berkeley, California.
[45] Der E-Modul von Seilen unter Berücksichtigung des Durchhangs. Der Bauingenieur. 1997;40(2):52-5.
[46] Aviram A, Mackie KR, Stojadinović B. Guidelines for nonlinear analysis of bridge structures in California. PEER Report 2008/03. Berkeley, USA: Pacific Earthquake Engineering Research Center, University of California; 2008.
[47] Zona A, Ragni L, Dall'Asta A. Simplified method for the analysis of externally prestressed steel-concrete composite beams. J Constr Steel Res 2009;65(2):308-31.
[48] Nielson BG. Analytical fragility curves for highway bridges in moderate seismic zones. Phd. Dissertation, Georgia Institute of Technology.
[49] Guo A, Shen Y, Bai J, Li H. Application of the endurance time method to the seismic analysis and evaluation of highway bridges considering pounding effects. Eng Struct 2017;131:220-30.
[50] Zhang H, Li J, Saidi MS. Evaluation of performance of a skew bridge in Wenchuan 2008 earthquake. Proceedings of the International Symposium on Engineering Lessons Learned from the 2011 Great East Japan, Tokyo, Japan; 2012.
[51] Gao Y, Yuan W, Jin X. Soil-structure-water intercation of a cable-stayed bridge under seismic excitation. The 14th world conference on earthquake engineering, Bejing, China; 2008.
[52] Shakya K, Wijeyewickrema AC. Mid-column pounding of multi-story reinforced concrete buildings considering soil effects. Adv Struct Eng 2009;12(1):71-85.
[53] Anagnostopoulos SA. Pounding of buildings in series during earthquakes. Earthq Eng Struct Dyn 1988;16(3):443-56.
[54] Li Z, Yue F, Zhou L. Equivalent kelvin impact model for pounding analysis of bridges during earthquake. Eng Mech 2008;25(4):128-33. (in Chinese)
[55] Lankarani HM, Nikravesh PE. A contact force model with hysteresis damping for impact analysis of multibody systems. J Mech Des 1990;112(3):369-76.
[56] Muthukumar S, DesRoches R. A Hertz contact model with non-linear damping for pounding simulation. Earthq Eng Struct Dyn 2006;35:811-28.
[57] Chopra AK. Dynamics of Structures: Theory and applications to earthquake engineering. Prentice-Hall: Englewood Cliffs, NJ, 1995.

[58] Xu Y, Tong C, Li J. Simplified calculation method for supplemental viscous dampers of cable-stayed bridges under near-fault ground motions. J Earthq Eng 2018;25:65-81.
[59] Anagnostopoulos SA. Pounding of buildings in series during earthquakes. Earthq Eng Struct Dyn 1988;16:443-56.
[60] Azevedo J, Bento R. Design criteria for buildings subjected to pounding. Eleventh World Conference on Earthquake Engineering, Acapulco, Mexico; 1996.
[61] Guo A, Cui L, Li H. Stiffness of the contact-element models for the pounding analysis of highway bridges: Experimental evaluation. J Earthq Eng 2012;16:1132-60.
[62] Vamvatsikos D, Cornell CA. Incremental dynamic analysis. Earthq Eng Struct Dyn 2002;31(3):491-514.
[63] Baker JW. Efficient analytical fragility function fitting using dynamic structural analysis. Earthq Spectra 2015;31(1):579-99.
[64] FEMA Hazus-MH MR5. Multi-hazard loss estimation methodology: earthquake model, HAZUS-MH MR5: Technical manual. Washington DC: Federal Emergency Management Agency; 2011.
[65] Choi E, DesRoches R, Nielson B. Seismic fragility of typical bridges in moderate seismic zones. Eng Struct 2004;26(2):187-99.
[66] Pang Y, Wu X, Shen G, Yuan W. Seismic fragility analysis of cable-stayed bridges considering different sources of uncertainties. J Bridge Eng 2014;19(4):04013015.
[67] Sharbati R, Rahimi R, Koopialipoor MR, et al. Detection and extraction of velocity pulses of near-fault ground motions using asymmetric Gaussian chirplet model. Soil Dyn Earthq Eng 2020;133:106123.
[68] Zahrah TF, Hall WJ. Earthquake energy absorption in SDOF structures. J Struct Eng 1984; 110(8):1757-72.
[69] Kuwamura H, Galambos TV. Earthquake load for structural reliability. J Struct Eng 1989;115(6):1446-62.